High resolution foreground cleaned CMB map from WMAP

Max Tegmark* and Angélica de Oliveira-Costa
Department of Physics & Astronomy, University of Pennsylvania, Philadelphia, Pennsylvania 19104, USA

Andrew J. S. Hamilton†
JILA and Department of Astrophysical and Planetary Sciences, University of Colorado, Boulder, Colorado 80309, USA

(Received 4 March 2003; published 29 December 2003)

We perform an independent foreground analysis of the Wilkinson Microwave Anisotropy Probe (WMAP) maps to produce a cleaned cosmic microwave background (CMB) map (available online) useful for cross-correlation with, e.g., galaxy and x-ray maps. We use a variant of the Tegmark-Efstathiou technique that assumes that the CMB has a blackbody spectrum, but is otherwise completely blind, making no assumptions about the CMB power spectrum, the foregrounds, WMAP detector noise or external templates. Compared with the foreground-cleaned internal linear combination map produced by the WMAP team, our map has the advantage of containing less non-CMB power (from foregrounds and detector noise) outside the Galactic plane. The difference is most important on the angular scale of the first acoustic peak and below, since our cleaned map is at the highest $(12.6')$ rather than lowest $(49.2')$ WMAP resolution. We also produce a Wiener filtered CMB map, representing our best guess as to what the CMB sky actually looks like, as well as CMB-free maps at the five WMAP frequencies useful for foreground studies. We argue that our CMB map is clean enough that the lowest multipoles can be measured without any galaxy cut, and obtain a quadrupole value that is slightly less low than that from the cut-sky WMAP team analysis. This can be understood from a map of the CMB quadrupole, which shows much of its power falling within the Galaxy cut region, seemingly coincidentally. Intriguingly, both the quadrupole and the octopole are seen to have power suppressed along a particular spatial axis, which lines up between the two, roughly towards $(l,b)\sim(-110°,60°)$ in Virgo.

DOI: 10.1103/PhysRevD.68.123523 PACS number(s): 98.80.Es

I. INTRODUCTION

The release of the first results [1–18] from the Wilkinson Microwave Anisotropy Probe (WMAP) constituted a major milestone in cosmology, laying a solid foundation upon which to found the cosmological quest in the coming years. Although much of the attention in the wake of the WMAP release has focused on the power spectrum and its cosmological implications, the primary stated science goal of WMAP is to produce maps. Indeed, one of the qualitatively new types of research made possible by WMAP involves taking advantage of this spatial information by cross-correlating the maps with other cosmological templates such as galaxy [19], x-ray [20,21], infrared and lensing maps [22], which can reveal interesting signals ranging from the late integrated Sachs-Wolfe effect to the Sunyaev-Zel'dovich (SZ) effect and lensing [23,24].

Many such future studies will be looking for signals of modest statistical significance, so it is important to quantify and minimize unwanted signals in the map due to foreground contamination and detector noise. Accurately understanding the foreground signal is also important for the interpretation of the WMAP early reionization detection [1,15,17,25–27] and for the interpretation of the low WMAP quadrupole [1,6,17], since Galactic foregrounds are most important on large angular scales [28,30]. The WMAP team has already performed a careful foreground analysis [3] combining the five frequency bands into a single foreground-cleaned map, shown in Fig. 1 (top). Given the huge effort that has gone into creating the spectacular multifrequency maps, it is clearly worthwhile to subject them to an independent foreground analysis. This is the purpose of the present paper, which we will argue not only corroborates the findings of the WMAP team, but also makes some further improvements that we believe are useful.

The main goal of this paper is to remove foregrounds, not to understand or model them. For reviews of foreground modeling issues, see, e.g., [3,28–41] and references therein. There is a rich literature of techniques for foreground removal. The work most closely related to the present paper is that done in preparation for the Planck mission [33–35], developing multipole-based cleaning techniques and testing them on simulations.

II. ANALYSIS AND RESULTS

A. The problem

A key goal of the cosmic microwave background (CMB) community is to measure the function $x(\hat{\mathbf{r}})$, the true CMB sky temperature in the sky direction given by the unit vector $\hat{\mathbf{r}}$. The WMAP team have observed the sky in five frequency bands denoted K, Ka, Q, V and W, centered on the frequencies of 22.8, 33.0, 40.7, 60.8 and 93.5 GHz, respectively, producing five corresponding maps (Fig. 2, left) that we will refer to as $\mathbf{y}_i$, $i=1,\ldots,5$. In practice, each of these maps are discretized into $n=12\times512^2=3\,145\,728$ HEALPIX[1] pixels

*Email address: max@physics.upenn.edu
†Email address: Andrew.Hamilton@colorado.edu

[1]The HEALPIX package is available from http://www.eso.org/science/healpix/.

 ©2003 The American Physical Society

[42,43], so $\mathbf{y}_i$ is an n-dimensional vector. However, since the maps are more than adequately oversampled relative to the beam resolution, it is equivalent and often simpler to think of them simply as five smooth functions $y_i(\hat{\mathbf{r}})$. Conversely, we will occasionally write the true sky as a pixelized vector $\mathbf{x}$.

These maps are related to the true sky $\mathbf{x}$ by the affine relation

$$\mathbf{y}_i = \mathbf{A}_i \mathbf{x} + \mathbf{n}_i, \tag{1}$$

where the matrix $\mathbf{A}_i$ encodes the effect of beam smoothing and the additive term $\mathbf{n}_i$ is the contribution from detector noise and foreground contamination, collectively referred to as "junk" below since it complicates the recovery of $\mathbf{x}$. Defining the larger matrices and vectors

$$\mathbf{A} \equiv \begin{pmatrix} \mathbf{A}_1 \\ \vdots \\ \mathbf{A}_5 \end{pmatrix}, \quad \mathbf{y} \equiv \begin{pmatrix} \mathbf{y}_1 \\ \vdots \\ \mathbf{y}_5 \end{pmatrix}, \quad \mathbf{n} \equiv \begin{pmatrix} \mathbf{n}_1 \\ \vdots \\ \mathbf{n}_5 \end{pmatrix}, \tag{2}$$

we can rewrite the system of equations given by Eq. (1) as

$$\mathbf{y} = \mathbf{A}\mathbf{x} + \mathbf{n}, \tag{3}$$

a set of linear equations that would be highly overdetermined by a factor five if it were not for the presence of unknown junk $\mathbf{n}$.

Foreground removal involves inverting this overdetermined system of noisy linear equations. The most general linear[2] estimate of $\tilde{\mathbf{x}}$ of the true sky $\mathbf{x}$ can be written

$$\tilde{\mathbf{x}} = \mathbf{W}\mathbf{y} \tag{4}$$

for some $n \times (5n)$ matrix $\mathbf{W}$. We will require that the inversion leaves the true sky unaffected, i.e., that the expected measurement error $\langle \tilde{\mathbf{x}} \rangle - \mathbf{x}$ is independent of $\mathbf{x}$. Bennett *et al.* [3] refer to this property as the inversion having unit response to the CMB. Methods involving maximum-entropy reconstruction or some form of smoothing typically lack this property. Substituting Eq. (3) into Eq. (4) shows that this requirement corresponds to the constraint

$$\mathbf{W}\mathbf{A} = \mathbf{I}. \tag{5}$$

B. The mathematically optimal solution

Which choice of $\mathbf{W}$ gives the smallest rms errors from foregrounds and detector noise combined? Physically different but mathematically identical problems were solved in a CMB context by [44,45], showing that the minimum-variance choice is

$$\tilde{\mathbf{x}} = [\mathbf{A}^t \mathbf{N}^{-1} \mathbf{A}]^{-1} \mathbf{A}^t \mathbf{N}^{-1} \mathbf{y}, \tag{6}$$

where $\mathbf{N} \equiv \langle \mathbf{n}\mathbf{n}^t \rangle$. For an extensive discussion of different methods proposed in the literature and the relations between them, see [29]. Although optimal, this method is unfortunately unfeasible for the WMAP case, for two reasons. First, it requires the inversion of the $(5n) \times (5n)$ matrix $\mathbf{N}$. Although the detector noise contribution to this matrix is close to diagonal for WMAP, the foreground contribution is certainly not. Second, it requires knowing the matrix $\mathbf{N}$, which has many more components than there are pixels in the map.

C. The WMAP team solution

In producing their internal linear combination (ILC) map, the WMAP team adopt a simpler approach [3], first smoothing all five maps to a common angular resolution of 1° and then performing the cleaning separately for each pixel. The smoothing implies that $\mathbf{A}_i = \mathbf{I}$ (if we redefine $\mathbf{x}$ to be the true sky smoothed to 1°), and Eq. (4) reduces to the simple form

$$\tilde{\mathbf{x}}(\hat{\mathbf{r}}) = \sum w_i \mathbf{y}_i(\hat{\mathbf{r}}) \tag{7}$$

for five weights w_i that according to Eq. (5) must sum to unity. The WMAP team chose the weights that minimize the rms fluctuations in the cleaned map $\tilde{\mathbf{x}}$, using 12 separate weight vectors for 12 disjoint sky regions.

Although this method works well, it can be improved by allowing the weights to depend on angular scale (i.e. on harmonic number ℓ) as well as on Galactic latitude. This has two advantages. First, the angular resolution is limited not by that of the lowest resolution channel [the K-band full width at half maximum (FWHM) is 49.2′], but rather by that of the highest resolution channel (the W-band FWHM is 12.6′). Second, as shown by [28], letting the weights depend on angular scale produces a cleaner map by taking into account that the frequency dependence of the unwanted signals varies with scale: at large scales, galactic foregrounds dominate, whereas at small scales, detector noise dominates.

D. Our solution

In this paper, we will take an approach intermediate between the two described above, aiming to approximate the optimal method while staying within the realm of numerical feasibility. Our method is essentially that of Tegmark and Efstathiou [28], implemented to make it blind and free of assumptions both about the CMB power spectrum and about foreground and noise properties. The only assumption, which is crucial, is that the CMB has the blackbody spectrum determined by the COBE/FIRAS experiment [60]. The method strictly respects the requirement of Eq. (5), which is most easily seen by verifying that each of the steps described below do so individually. The gist of our method is to combine the five WMAP bands with weights that depend both on angular scale and on distance to the Galactic plane (we subdivide the sky into 9 regions of decreasing overall cleanliness). We begin by describing the angular scale separation, then turn to the spatial subdivision in Sec. II F.

[2]In addition to simplicity and transparency, linear methods have the advantage that the noise properties of $\tilde{\mathbf{x}}$ can be readily calculated from those of the input maps.

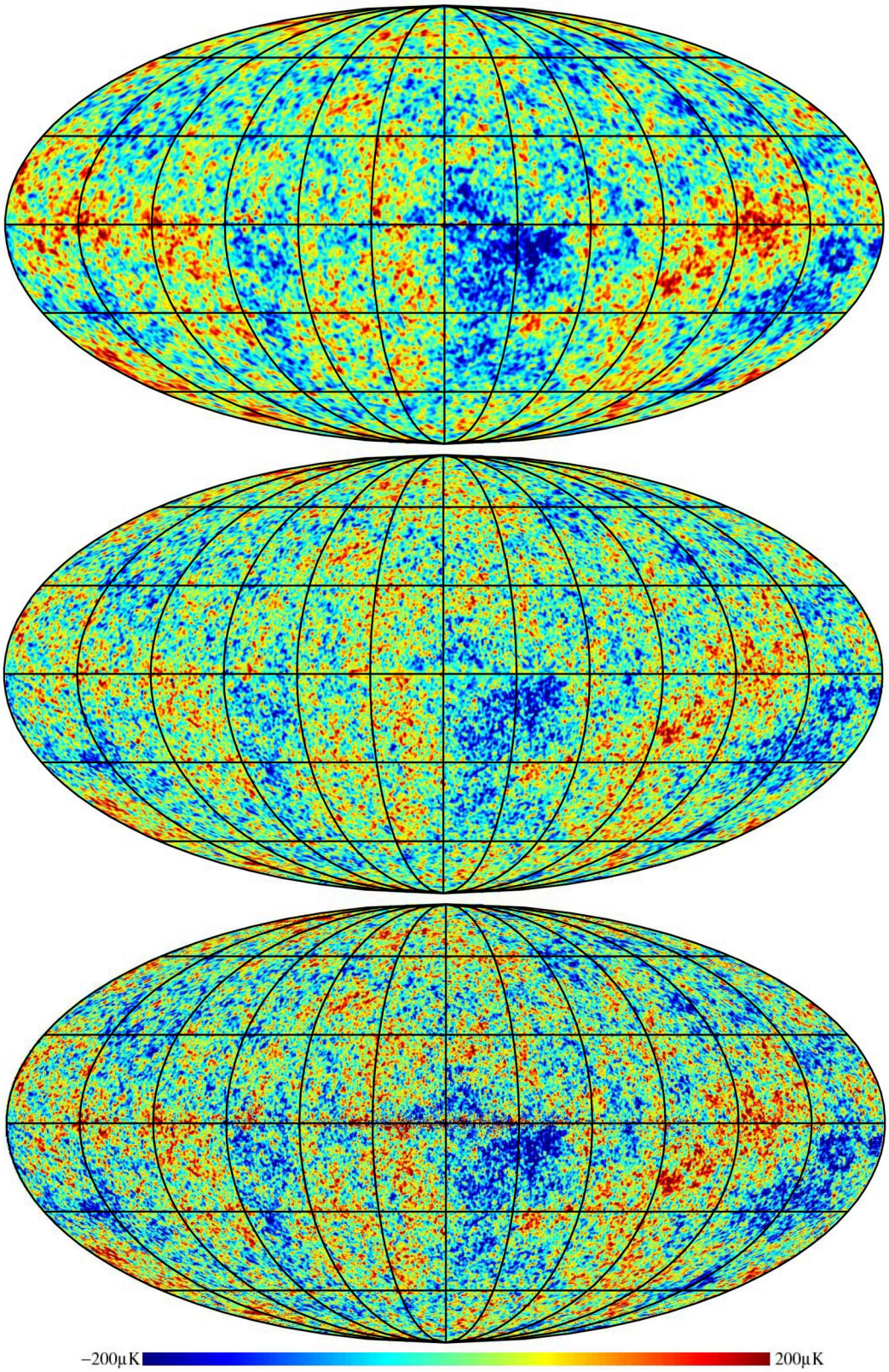

FIG. 1. The linearly cleaned WMAP team map (top), our Wiener filtered map (middle) and our raw map (bottom). Here and throughout, all maps are shown in Mollweide projection in Galactic coordinates with the Galactic center $(l,b)=(0,0)$ in the middle and Galactic longitude l increasing to the left.

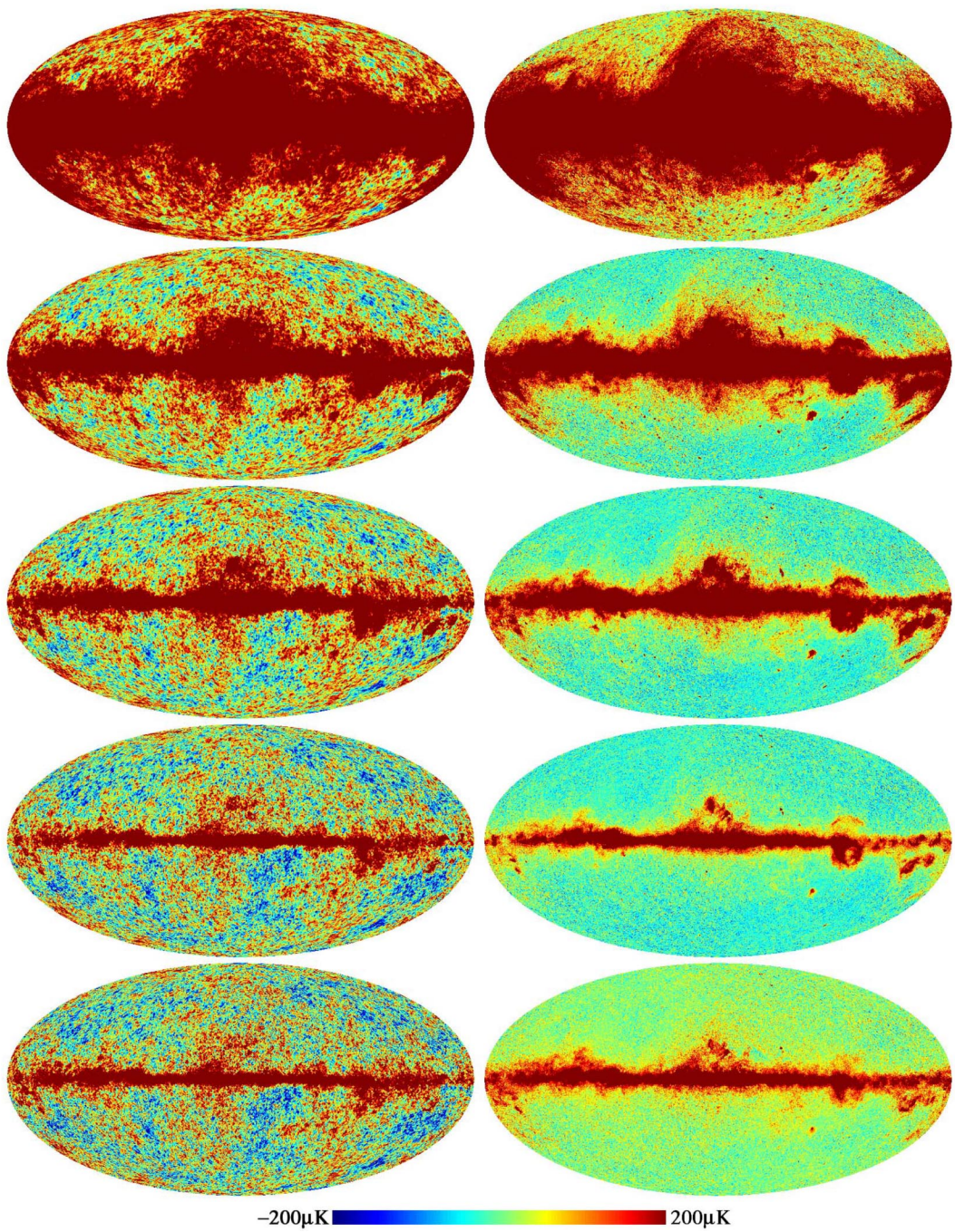

FIG. 2. The five WMAP frequency bands K, Ka, Q, V and W (top to bottom) before (left) and after (right) removing the CMB.

We perform our cleaning in multipole space as in [28], and go back and forth between spherical harmonic coefficients

$$a^i_{\ell m} \equiv \int Y_{\ell m}(\hat{\mathbf{r}})^* \mathbf{x}_i(\hat{\mathbf{r}}) d\Omega \tag{8}$$

and real-space maps

$$x_i(\hat{\mathbf{r}}) = \sum a^i_{\ell m} Y_{\ell m}(\hat{\mathbf{r}}) \tag{9}$$

using the HEALPIX package [42,43] with $\ell_{\max} = 1024$. Since this employs a spherical harmonic transform algorithm using fast Fourier transforms in the azimuthal direction [46], each transformation takes only about a minute on a Linux workstation. Each cleaned map is defined by

$$a_{\ell m} \equiv \sum_{i=1}^{5} w^i_\ell \frac{a^i_{\ell m}}{B^i_\ell} \tag{10}$$

for some set of five-dimensional weight vectors $\mathbf{w}_\ell$, where B^i_ℓ is the beam function for the ith channel from [14]. (There

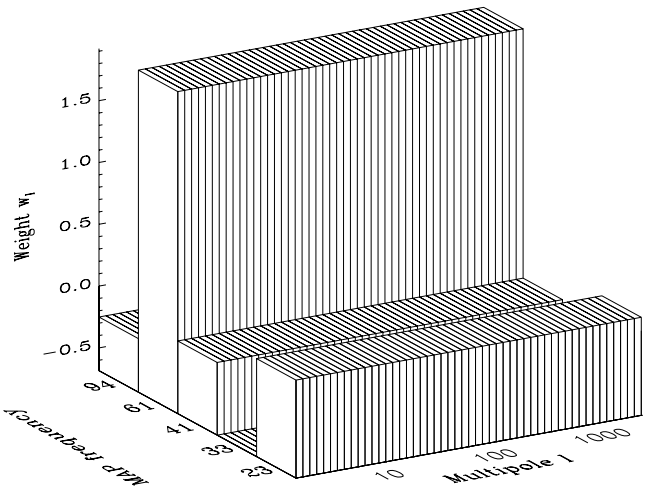

FIG. 3. The weights $\mathbf{w}_\ell$ used to create the internal linear combination map of the WMAP team are independent of angular scale. The figure shows the weights $\mathbf{w}_\ell = (0.109, -0.684, -0.096, 1.921, -0.250)$ used outside of the galactic plane.

are 4 W-band maps, 2 V-band maps and 2 Q-band maps; we combine these into single maps at each frequency by straight averaging and therefore average the corresponding beam functions as well.) When computing our final cleaned map in real space, we multiply $a^i_{\ell m}$ by B^5_ℓ in Eq. (9) so that it has the beam corresponding to the highest-resolution WMAP band.

To gain intuition for the weight vectors $\mathbf{w}_\ell$ that specify a cleaned map, we have plotted them for four interesting cases in Figs. 3, 4, 5 and 6. Figure 3 corresponds to the weighting used by the WMAP team for the region away from the galactic plane, and is simply independent of ℓ. To recover their published internal linear combination map shown in Fig. 1 (top), one simply applies these weights after first multiplying each $a^i_{\ell m}$ by a Gaussian beam with FWHM$=1°$ in Eq. (9).

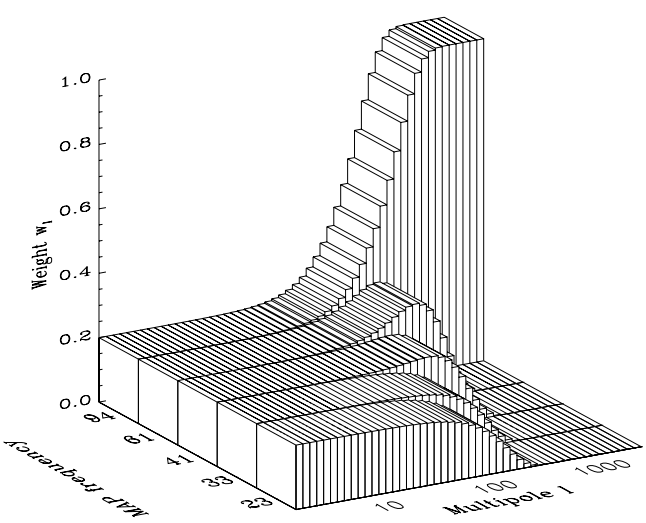

FIG. 4. If there were no foregrounds and equal noise in the five input maps, then equal weighting at low ℓ would give way to favoring the highest resolution bands at high ℓ. This example uses the forecast WMAP beam and noise specifications from [29] rather than the actual ones.

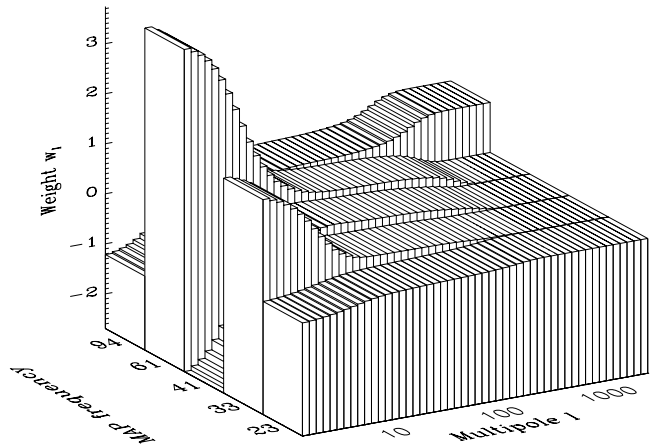

FIG. 5. The optimal WMAP weights forecast by [29] for the middle-of-the-road foreground model from [29].

The main drawback of this weighting is that it neglects that there is a tradeoff between foregrounds and detector noise which depends strongly on angular scale. Diffuse foregrounds are most important on large scales where detector noise is negligible, warranting large negative and positive weights to aggressively subtract foregrounds. Detector noise, on the other hand, is most important on small scales, both because of its Poissonian nature the (power spectrum C_l roughly constant in the observed map) and because the beam correction in Eq. (10) causes it to blow up exponentially on scales smaller than the angular resolution [28,47]. In the limit $\ell \to \infty$, the best weighting is therefore $\mathbf{w}_\ell \to (0,0,0,0,1)$ regardless of what the foregrounds are doing, as illustrated in Fig. 4, since the W-band has the best resolution.

We choose to minimize the total unwanted power from foregrounds and noise combined, separately for each harmonic ℓ as in [28], as opposed to only for the combination corresponding to the 1° pixel variance as in [3]. As seen in Fig. 5, one expects such a weighting to combine features

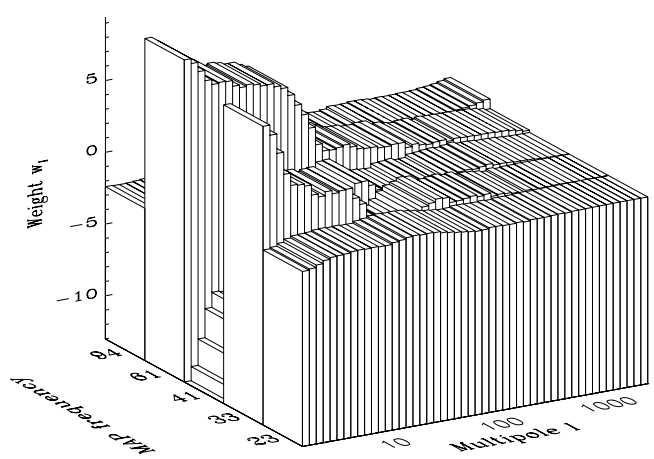

FIG. 6. The actual weights we use for the 3rd cleanest of the 9 sky regions shown in Fig. 8. The dirtier the sky region, the more aggressive the weighting becomes, using large negative and positive values to subtract foregrounds.

from the two previous figures: rather aggressive subtraction using all five channels at low ℓ, more cautious subtraction using only the higher-resolution channels on intermediate scales, and all the weight on the W-band at extremely high ℓ. In particular, it is crucial to downweight the K-band when cleaning on the scales of the acoustic peaks, otherwise the acoustic peaks in the resulting map will be dominated by K-band noise.

The constraint equation (5) that we leave the CMB untouched corresponds to the requirement that the weights sum to unity ($\Sigma_i \mathbf{w}_\ell^i = 1$) for each ℓ, i.e., that

$$\mathbf{e}\cdot\mathbf{w}_\ell = 1, \tag{11}$$

where $\mathbf{e}=(1,1,1,1,1)$ is a column vector of all ones. Minimizing the power $\langle |a_{\ell m}|^2\rangle$ in the cleaned map of Eq. (10) subject to this constraint gives [28,29,48]

$$\mathbf{w}_\ell = \frac{\mathbf{C}_\ell^{-1}\mathbf{e}}{\mathbf{e}^t\mathbf{C}_\ell^{-1}\mathbf{e}}, \tag{12}$$

where $\mathbf{C}_\ell$ is the 5×5 matrix-valued cross-power spectrum

$$\mathbf{C}_\ell^{ij} \equiv \langle a_{\ell m}^{i} {}^{*} a_{\ell m}^{j}\rangle. \tag{13}$$

As an example, Fig. 6 shows the weights we obtain for the 3rd cleanest of the 9 sky regions shown in Fig. 8 below. We see that just as forecast in Fig. 5, and as in the WMAP team weighting of Fig. 3, the 61 GHz V channel is "the breadwinner," getting a large positive weight on large scales since it has the lowest overall foreground level. The 94 GHz W channel gets a negative weight to subtract out dust, and the three lower frequency channels are used to subtract out synchrotron, free-free and any other emission dominating at low frequencies. In cleaner sky regions, weights get less aggressive in the sense of acquiring smaller absolute values. In particular, we recover weights similar to those of the WMAP team (Fig. 3) on large scales for the Kp2 sky cut defined and used by [3].

E. Blind analysis and the power spectrum matrix

We compute the power spectrum matrix $\mathbf{C}_l$ in practice using the method of [49]; a similar approach was used by the BOOMERANG [50] and WMAP [6] teams. This simply consists of expanding the masked sky patch in question in spherical harmonics and then correcting for window function effects. Our only variation is that we do not invert the window matrix to obtain anticorrelated band power estimates with delta function window functions. Rather, we simply divide the quadratic estimators by the area of the window δT_ℓ^2 window functions, which asymptotes to the unbiased minimum variance estimators of [51] on scales much smaller than the sky patch analyzed. An example of our window functions is shown in Fig. 7.

As an example, Fig. 9 shows the measured power spectrum for the V-band, the cleanest of WMAP's frequency bands.

One fact worth emphasizing is that our weighting scheme of Eq. (12) is totally blind, assuming nothing whatsoever

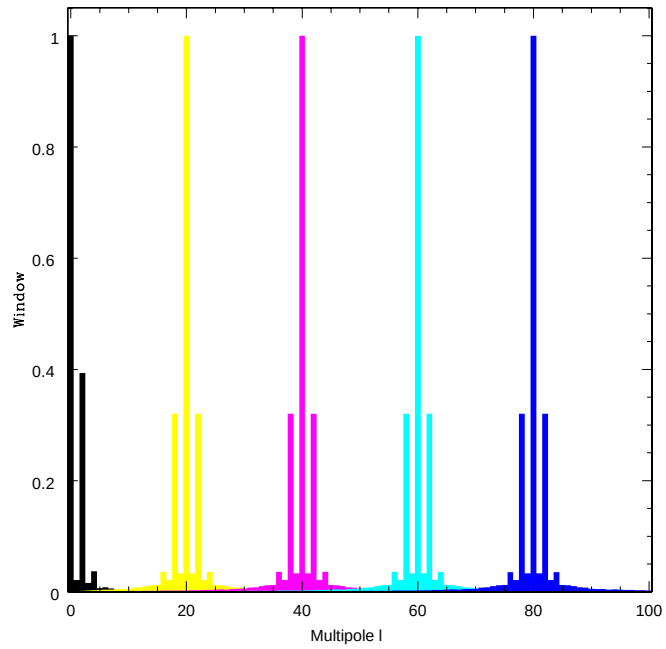

FIG. 7. Sample band power window functions are shown for the cleanest of the sky regions from Fig. 8, all normalized so that the maximum value is unity. The approximate lack of leakage from odd numbers of multipoles away results from the approximate parity symmetry of this region.

about the CMB power spectrum, the foregrounds, the WMAP detector noise or external templates. The only assumption is that the CMB spectrum is the blackbody that the WMAP team have modeled it as, so that the CMB contributes equally to all five channels—otherwise the vector $\mathbf{e}$ would be replaced by some other constant vector. We see that there is no need to model the CMB, the foregrounds or the noise, since all we need for computing the optimal weights is the *total* power spectrum matrix $\mathbf{C}_l$, containing the total contribution from CMB, foregrounds and noise combined— and this can be measured directly from the data.

We can decompose $\mathbf{C}_l$ as a sum of two terms,

$$\mathbf{C}_\ell = \mathbf{C}_\ell^{\rm junk} + \mathbf{C}_\ell^{\rm cmb} = \mathbf{C}_\ell^{\rm junk} + C_\ell^{\rm cmb}\mathbf{e}\mathbf{e}^t, \tag{14}$$

where the second term is the CMB contribution and the first term is the contribution from noise and foregrounds. Note that if we keep $\mathbf{C}_\ell^{\rm junk}$ fixed and change $C_\ell^{\rm cmb}$, the weights given by Eq. (12) stay the same. The easiest way to see this is to note that the quantity we are minimizing is $\langle |a_{\ell m}|^2\rangle = \mathbf{w}^t C_\ell \mathbf{w} = \mathbf{w}^t\mathbf{C}_\ell^{\rm junk}\mathbf{w} + C_\ell^{\rm cmb}(\mathbf{e}\cdot\mathbf{w})^2 = \mathbf{w}^t\mathbf{C}_\ell^{\rm junk}\mathbf{w} + C_\ell^{\rm cmb}$, so the CMB power is just an additive constant that does not affect the optimal weighting. This means that our method is blind to assumptions about the underlying (ensemble-averaged) CMB power spectrum. Although we will return below in Sec. II G to the issue of how to determine what fraction of the power $\mathbf{C}_\ell$ comes from each of the two terms in Eq. (14), it is important to remember that this affects only the physical interpretation, not our cleaning method and the maps we produce.

F. Subdividing the sky

To minimize the variance in our cleaned map, we should take advantage of all ways in which the unwanted signals (noise and foregrounds) differ from the CMB in their contribution to the covariance matrix $\mathbf{N}$ in Eq. (6). Above we exploited their different dependence on angular scale ℓ. Unlike the CMB, foregrounds are not an isotropic Gaussian random field. Rather, their variance differs dramatically between clean and dirty regions of the sky. It is therefore desirable to subdivide the sky into a set of regions of increasing cleanliness and perform the cleaning separately for each one [28]. One then expects our method described above to settle on more aggressive weights for the dirtier regions, where foregrounds are much more of a concern than noise. A second advantage of such a subdivision is that the frequency dependence of the foregrounds is likely to differ between very dirty and very clean regions, again resulting in different optimal weights. The WMAP team used the latter argument to motivate their subdivision of the sky into 12 regions, and convincingly demonstrated that foreground spectra indeed did vary across the sky, notably for synchrotron radiation where the spectrum was found to steepen towards increasing galactic latitudes.

The WMAP team have created a set of sky-masks of increasing cleanliness based solely the K-band map. Although these masks are undoubtedly fine in practice, the procedure used in creating them is not blind, since it rests on the assumption that all dirty regions are dirty in the K-band. In particular, if a foreground manifests itself only at higher frequencies (imagine, say, a blob with localized dust emission without detectable synchrotron or free-free emission), it would go unnoticed. A second minor drawback of this K-band approach is that random CMB fluctuations affect the masks at a low level. In other words, the mask was based on the upper left map in Fig. 2 which, as opposed to the upper right map, contains CMB fluctuations.

To preserve the blind nature of our method, we therefore create sky masks with a different procedure. We first form four difference maps W-V, V-Q, Q-K and K-Ka, thereby obtaining maps guaranteed to be free of CMB signal that pick up any signals with a non-CMB spectrum. We then form a combined "junk map" by taking the largest absolute value of these four maps at each point in the sky (Fig. 8, top). Finally, we create disjoint sky regions based on contour plots of this map. We use cuts that are roughly equispaced on a logarithmic scale, corresponding to thresholds of 30000, 10000, 3000, 1000, 300 and 100 μK (Fig. 8, bottom). We emphasize that we have found no evidence whatsoever for any actual problems with the WMAP team masks, and opt to use our own simply to preserve the blind and CMB-independent nature of our analysis. As a cross-check, we also repeated our entire analysis using the WMAP masks Kp0, Lp2 and Kp12, obtaining similar results.

We followed the WMAP team procedure in the details of converting the contours into the masks shown in Fig. 8 (bottom): we downsampled the junk map to HEALPIX resolution 64, imposed the cuts, went back up to HEALPIX resolution 512, performed Gaussian smoothing with FWHM$=2°$ on the $\{0,1\}$-valued mask and imposed a cutoff of 0.5. The WMAP team reported strong spatial variations of foreground spectra in the innermost parts of the galactic plane, and therefore subdivided this into 11 disjoint regions. We were unable to reproduce this procedure since they did not specify which these regions were. Instead, we merely lopped off three spatially disconnected islands in the two dirtiest regions as their own separate masks, as illustrated in Fig. 8 (bottom), leaving 9 separate masks in total.

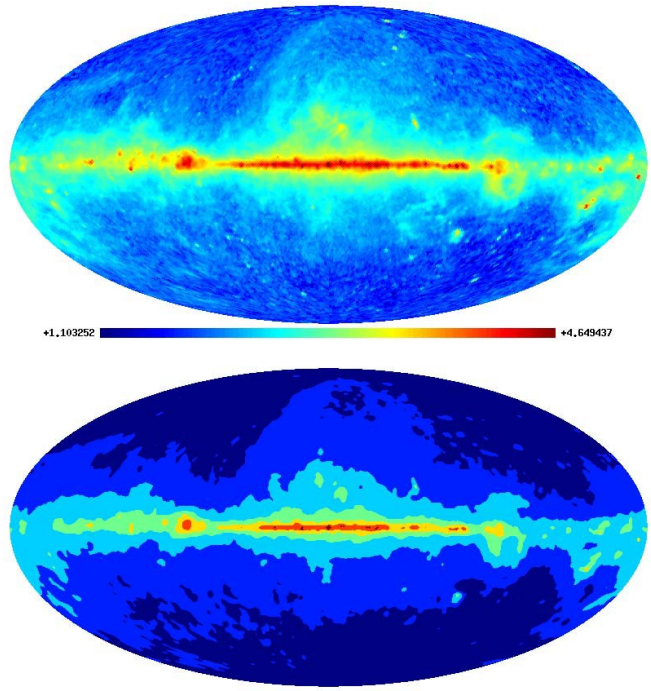

FIG. 8. The top panel shows our junk map with a color scale that is uniform in the logarithm of the temperature in μK. The bottom panel show our subdivision of the sky into seven regions of decreasing cleanliness. From outside in, they correspond to junk map temperatures $T<100$ μK, 100 μK$-$300 μK, 300 μK$-$1 mK, 1 mK$-$3 mK, 3 mK$-$10 mK, 10 mK$-$30 mK and $T>30$ mK, respectively. The last of these regions contains only the set of roundish blobs in the inner Galactic plane. The second dirtiest region is seen to be topologically disconnected, and we treat its leftmost and rightmost blobs as separate regions, giving nine regions in total.

Our multipole-based cleaning is nonlocal in the spirit of Eq. (4), and although it guarantees that the CMB signal is preserved separately for each pixel, this is of course not the case for foregrounds. To avoid mirages of foreground emission from the Galactic plane leaking up to high latitudes, we clean the galaxy "from inside out," i.e., clean the dirtiest region first, the second dirtiest region second, etc. To be specific, we start by defining five temporary maps, initially set equal to the five WMAP channels (Fig. 2, left). We then repeat the following cleaning procedure nine times, once corresponding to each region $i=1,\ldots,9$:

(i) Compute the power spectrum matrix $\mathbf{C}_\ell$ and the optimal weights $\mathbf{w}_\ell$ for the ith region only.

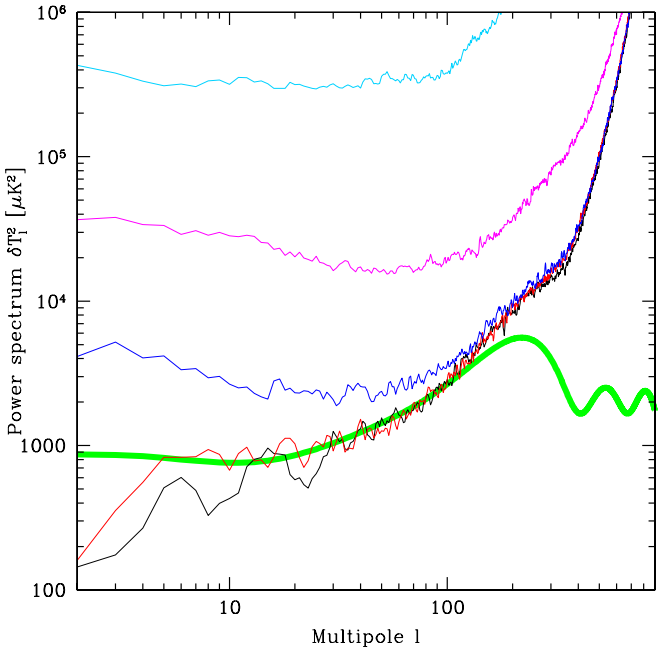

FIG. 9. Total power spectra for CMB, foregrounds and noise combined are shown for the 61 GHz V-band, the one with the overall lowest foreground levels. This is the (4,4) element of the power spectrum matrix $\mathbf{C}_\ell$. From bottom to top, they correspond to the five cleanest sky regions shown in Fig. 8. For comparison, the thick curve shows the best-fit CMB model from [17,18].

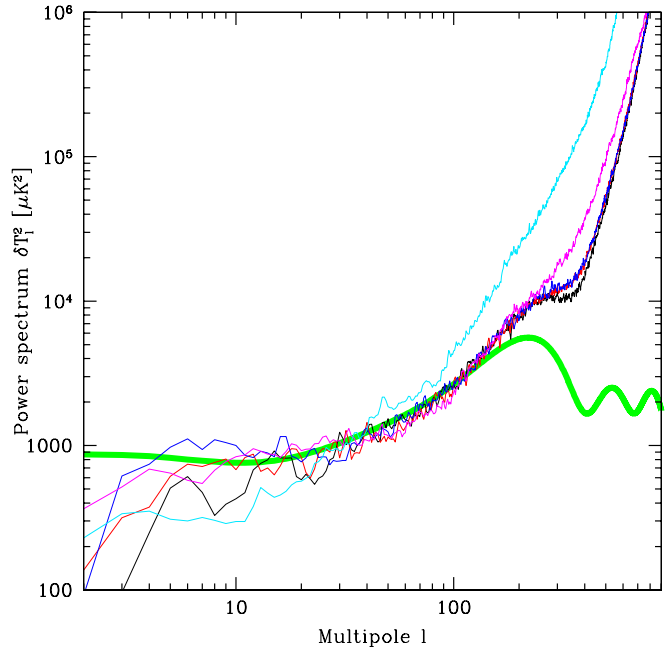

FIG. 10. Same as previous figure, but for our foreground-cleaned CMB map (bottom panel of Fig. 1). The power spectra of the cleanest sky regions are seen to be virtually identical with those for V-band on large scales, showing how subdominant smooth foregrounds are at 61 GHz.

(ii) Expand the five temporary maps in spherical harmonics and compute a cleaned all-sky map using the weights from step (i).

(iii) Replace the ith region of the temporary maps by the corresponding region in the cleaned map from step (ii) (smoothed to the resolution appropriate for that channel, of course, by multiplying by B_ℓ^i in ℓ space).

Visually, one thus sees the foreground contamination gradually being cleaned off from Fig. 2 as this iteration proceeds, starting in the inner Galactic plane and proceeding outward. At the end of the nine iterations, the five temporary maps equal the desired cleaned map at the K-, Ka-, Q-, V-, and W-band resolutions, respectively.

G. Interpretation of the cleaned maps

Figure 1 (bottom) shows our final cleaned map and Fig. 10 shows its power spectrum in sky regions of varying cleanliness. We plot all maps after 21′ Gaussian smoothing (giving a net FWHM of 24′) to prevent them from being undersampled by the pixels in the image. The reader interested in using this map can download the corresponding 13 Megabyte HEALPIX fits file from the web.[3] To use this map, it is important to be clear on how to interpret it.

First of all, it is a sum of CMB, foreground and detector noise fluctuations. Although it was constructed by minimizing its power spectrum $C_\ell^{\rm clean}=\mathbf{w}_\ell^t\mathbf{C}_\ell\mathbf{w}_\ell$, its power nonetheless gives a *lower* bound on the CMB power spectrum, since the minimization was performed subject to the constraint that the CMB be preserved; $\mathbf{e}\cdot\mathbf{w}=1$.[4]

So what fraction of the power seen in Fig. 10 is due to CMB, foregrounds and detector noise, respectively? Let us first get some rough estimates from the figures, then present more quantitative limits. Since this paper is focused on minimizing foregrounds, not on physically modeling them, the interested reader is referred to the detailed foreground study of the WMAP team [3] for more information.

The WMAP team cleverly eliminated the average noise contribution by using only cross-correlations between different differencing assemblies (DAs) to measure the power spectrum, and used a combination of sky cutting and foreground subtraction (with external templates) to minimize the foreground contribution. The best fit cosmological model [17,18] to their measured CMB power spectrum [6] is shown for comparison in Figs. 9 and 10. For $\ell\lesssim 100$, it is seen to agree well with the lower envelope of our curves in Fig. 9, suggesting that foregrounds are subdominant in the cleanest parts of the 61 GHz sky. Figure 10 shows no noticeable

[3]Our cleaned maps are available for download at http://www.hep.upen.edu/~max/wmap.html, together with a high-resolution version of this paper.

[4]The only way in which its power could be biased low would be if random fluctuations in our estimate of the $\mathbf{C}_\ell$ matrix conspired to remove power. Although we found no indication of this actually happening, we computed our weights $\mathbf{w}_\ell$ using a heavily smoothed version of $\mathbf{C}_\ell$-matrix as a precaution. Specifically, we smooth over at least $\Delta\ell=10$ or 100 (ℓ,m)-modes, whichever is larger, obtaining an ℓ-dependence of $\mathbf{C}_\ell$ with no visible trace of random fluctuations.

excess power at $\ell \lesssim 100$ due to foregrounds in the cleaned map in any of the four cleanest sky regions from Fig. 8, which together cover all but the very innermost Galactic plane.

The slight power deficit on the very largest scales has two causes: one is the low quadrupole, to which we return in Sec. III below, which pulls down neighboring band power estimates because the band-power window, illustrated in Fig. 7, contains small off-diagonal contributions. The second cause is that we have not corrected for the effects of monopole and dipole removal, which pulls down the power estimates on the scale of the sky patch in question (our method produces an unbiased CMB map regardless of what $\mathbf{C}_\ell$ we use in Eq. (12), so this merely raises the variance in the cleaned map above the optimal level). On smaller scales, detector noise starts to dominate, and is seen to push our curves way above the CMB curve. A worthwhile future project for further quantifying foregrounds would be to repeat our analysis with $\mathbf{C}_\ell$ estimated in a way that removes the detector noise contribution. For Q, V and W bands, which each have more than one DA, this can be done using cross-correlations. For the (1,1) and (2,2) components of $\mathbf{C}_\ell$ (the K and Ka power spectra), it would involve subtracting the noise power using the WMAP team's noise model.

We can, however, give some quantitative limits even based on our measured $\mathbf{C}_\ell$ alone. Grouping the five coefficients $a^i_{\ell m}$ into a five-dimensional vector $\mathbf{a}_{\ell m}$, Eq. (13) becomes simply $\mathbf{C}_\ell = \langle \mathbf{a}^*_{\ell m} \mathbf{a}^t_{\ell m} \rangle$, and the cleaning procedure can be written $a_{\ell m} = \mathbf{w} \cdot \mathbf{a}_{\ell m}$. Using Eq. (12) shows that the power in the cleaned map is

$$C_\ell^{\rm clean} = \frac{1}{\mathbf{e}^t \mathbf{C}_\ell^{-1} \mathbf{e}}. \tag{15}$$

By subtracting our cleaned map from the input map, we obtain maps shown in Fig. 2 (right). These are guaranteed to be free from CMB power, since the cleaned map preserves the CMB. Most likely, we have subtracted some foreground power too, so the five maps should be interpreted as placing lower limits on the foreground power. (As a toy example, imagine synchrotron, free-free and dust emission tracing each other perfectly; the sum of their three spectra can then be written as a constant, which our method will interpret as CMB, plus a non-negative residual, which our method will interpret as foregrounds.) Using Eq. (14), the covariance matrix of these five CMB-free "junk maps" is

$$\mathbf{C}_\ell^{\rm junk} \geqslant \mathbf{C}_\ell^{\rm nocmb} \equiv \mathbf{C}_\ell - C_\ell^{\rm clean} \mathbf{e}\mathbf{e}^t = \mathbf{\Pi}_\ell \mathbf{C}_\ell \mathbf{\Pi}_\ell^t, \tag{16}$$

where the projection matrix

$$\mathbf{\Pi}_\ell \equiv \mathbf{I} - \mathbf{e}\mathbf{w}_\ell^t \tag{17}$$

satisfies $\mathbf{\Pi}_\ell^2 = \mathbf{\Pi}_\ell$, $\mathbf{\Pi}_\ell \mathbf{e} = 0$ and $\mathbf{\Pi}_\ell^t \mathbf{w} = 0$ and can be interpreted as projecting out the CMB component. In this notation, the maps in Fig. 2 (right) are defined by simply $\mathbf{\Pi}_\ell \mathbf{a}_{\ell m}$. The inequality $\mathbf{C}_\ell^{\rm junk} \geqslant \mathbf{C}_\ell^{\rm nocmb}$ refers only to the diagonal elements of these matrices. The five diagonal elements of $\mathbf{C}_\ell^{\rm junk}$ are plotted in Fig. 11 for our cleanest sky region from Fig. 8.

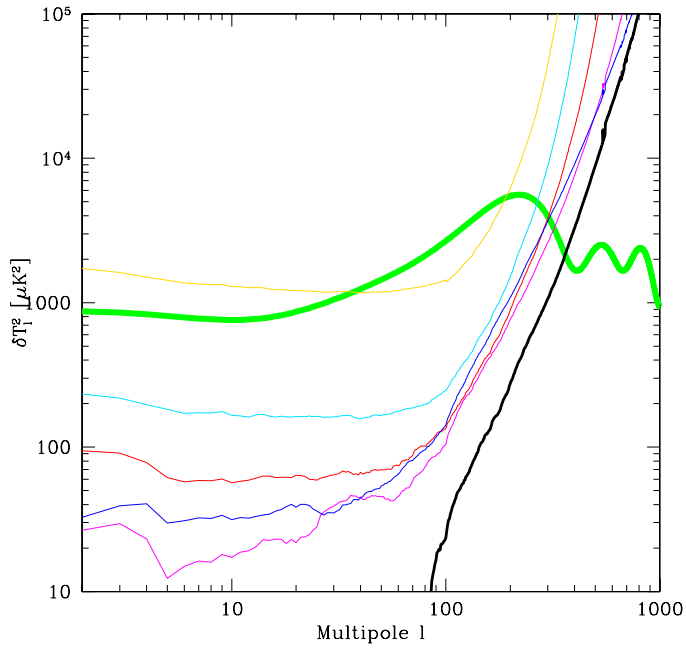

FIG. 11. Power spectra of non-CMB signals (foregrounds plus detector noise) in the cleanest part of the sky shown in Fig. 8. The five thin curves show the power spectra of five maps on the right side of Fig. 2, i.e., the five WMAP channels after our cleaned CMB map (Fig. 1, bottom) has been subtracted out. From top to bottom, the five curves correspond to 22.8, 33.0, 40.7, 93.5 and 60.8 GHz, respectively (note that the second highest frequency, V-band, is the cleanest). These curves should be interpreted as lower limits on foregrounds plus noise. The black curve gives the lower limit on foregrounds plus noise in our cleaned map using the method described in the text.

How much of $\mathbf{C}_\ell$ can possibly be due to CMB? In other words, forgetting for a moment about the weighting that gave Eq. (15), how large can we make $C_\ell^{\rm cmb}$ in Eq. (16) before the covariance matrix $\mathbf{C}_\ell^{\rm junk} = \mathbf{C}_\ell - \mathbf{C}_\ell^{\rm cmb} \mathbf{e}\mathbf{e}^t$ gets unphysical properties? First of all, no covariance matrix can have negative eigenvalues, so we must stop increasing $C_\ell^{\rm junk}$ once the smallest eigenvalue of $\mathbf{C}_\ell^{\rm junk}$ drops to zero. In fact, $\mathbf{\Pi}^t \mathbf{w} = 0$ implies that when using our optimal weighting and hence Eq. (15), $\mathbf{C}_\ell^{\rm junk}$ has a vanishing eigenvalue corresponding to the vector $\mathbf{w}$, and it is easy to show that this alternative method for estimating $C_\ell^{\rm cmb}$ is equivalent to our original method, being simply an alternative derivation of Eq. (15).

Let us now make a second assumption: that $\mathbf{C}_\ell^{\rm junk}$ cannot have any negative elements. The noise covariance matrix is guaranteed to have this property, since the absence of correlations between bands implies that it is diagonal. The foreground covariance matrix is also guaranteed to have this property if foreground emission is indeed *emission*, i.e., if foregrounds can make only positive contributions to the sky maps. Pure absorption at all frequencies likewise gives only positive correlations. This assumption, made also in the maximum-entropy analysis of [3], is likely to be valid at the WMAP frequencies, since the only known exception is the thermal SZ effect, and it changes sign only outside of the WMAP frequency range (around 217 GHz). In summary, we

therefore have two separate limits on the CMB power spectrum:

$$C_\ell^{\rm cmb} \leqslant C_\ell^{\rm clean}, \tag{18}$$

$$C_\ell^{\rm cmb} \leqslant \min_{i,j}(\mathbf{C}_\ell)_{ij}. \tag{19}$$

$C_\ell^{\rm clean}$ is also the actual variance of the cleaned map, so if the second limit is lower than first, then we know that the difference cannot be due to CMB.

To gain intuition, consider the following two examples of the junk+CMB decomposition of Eq. (14) for the simple case of only two frequency bands:

$$\mathbf{C}_\ell = \begin{pmatrix} 5 & 3 \\ 3 & 2 \end{pmatrix} = \begin{pmatrix} 4 & 2 \\ 2 & 1 \end{pmatrix} + \begin{pmatrix} 1 & 1 \\ 1 & 1 \end{pmatrix}, \tag{20}$$

$$\mathbf{C}_\ell = \begin{pmatrix} 2 & 1 \\ 1 & 2 \end{pmatrix} = \frac{1}{2}\begin{pmatrix} 1 & -1 \\ -1 & 1 \end{pmatrix} + \frac{3}{2}\begin{pmatrix} 1 & 1 \\ 1 & 1 \end{pmatrix} \tag{21}$$

$$= \begin{pmatrix} 1 & 0 \\ 0 & 1 \end{pmatrix} + \begin{pmatrix} 1 & 1 \\ 1 & 1 \end{pmatrix}. \tag{22}$$

In the first case, Eq. (15) gives $C_\ell^{\rm cmb}=1$, i.e., the largest contribution we can possible attribute to the CMB (the second term) is $\mathbf{e}\mathbf{e}^t$—if we scaled up the last term, then $\mathbf{C}_\ell^{\rm junk}$ (the first term) would acquire an unphysical negative eigenvalue. Moreover, we see that $\mathbf{C}_\ell^{\rm junk}$ looks like the covariance matrix of a perfectly respectable foreground, with a spectrum such that it contributes twice as high rms fluctuations to the first channel as to the second, and with perfect correlation between the two (the dimensionless correlation coefficient is $r=1$). Such a foreground would be completely removed by our method, and so we cannot place any lower limit on the foreground contribution to the cleaned map in this case. In the second case, Eq. (15) gives $C_\ell^{\rm cmb}=3/2$, so this will be the variance in the cleaned map. However, $\mathbf{C}_\ell^{\rm junk}$ (the first term) in Eq. (21) exhibits an unphysical anticorrelation between the two bands which neither noise nor foregrounds could produce, and Eq. (19) tells us that the CMB power $C_\ell^{\rm cmb} \leqslant 1$, corresponding to the alternative decomposition on the last line. This means that the junk map must have a power contribution of at least 1/2 which is not due to CMB.

This difference, which places a lower limit on the amount of non-CMB signal in our cleaned map, is shown as the black line in Fig. 11 for our actual five-band case. We see that although we get an interesting lower limit for $\ell > 100$, presumably dominated by detector noise, the residual foreground level is consistent with zero at low ℓ.

H. Wiener filtering

Figure 1 (bottom) shows our cleaned map of the CMB sky, and this is the map that should be used for cross-correlation analysis with other data sets and other scientific applications. For visualization purposes, however, we can do better. The ''best-guess'' map of what the CMB looks like, in the sense of minimizing the rms errors, is the Wiener filtered map defined by [52]

$$a_{\ell m}^{\rm Wiener} = \frac{C_\ell^{\rm cmb}}{C_\ell^{\rm clean}} a_{\ell m}. \tag{23}$$

This staple signal processing technique, multiplying by ''signal over signal plus noise,'' has additional attractive properties; for instance, it constitutes the best-guess (maximum posterior probability) map in the approximation of Gaussian fluctuations. Examples of recent applications of Wiener filtering to CMB and galaxy mapping include [53–59]. Our resulting Wiener filtered map is shown in Fig. 1 (middle), using the best fit model from the WMAP team [17,18] as our estimate of $C_\ell^{\rm cmb}$ in the numerator of Eq. (23). For the denominator, we take the larger of our measured $C_\ell^{\rm clean}$ and $C_\ell^{\rm cmb}$, so that the ratio is guaranteed to be $\leqslant 1$. The result is not an unbiased CMB map. Rather, Eq. (23) shows that each multipole gets multiplied by a number between 0 and 1, so features with high signal-to-noise are left unaffected whereas features that are not statistically significant become suppressed. This means that the features that one sees in Fig. 1 (middle) are likely to be real CMB fluctuations, having signal-to-noise exceeding unity.

The cleaned map at the bottom of Fig. 1 reveals some residual galactic fluctuations on very small angular scales, caused mainly by the fact that no other channels have fine enough angular resolution to help clean the W-band map for very large ℓ. We Wiener-filter each of the nine sky regions from Fig. 8 separately, so $C_\ell^{\rm clean}$ is much higher near the Galactic plane. This is why the Galactic contamination is imperceptible in the Wiener filtered map: Eq. (23) automatically suppresses fluctuations in regions with large residual foregrounds.

III. DISCUSSION

We have performed an independent foreground analysis of the WMAP maps to produce a cleaned CMB map. The only assumption underlying our method is that the CMB contributes equally to all five channels. This assumption rests on very solid ground [1]. The basic reason for this is that the COBE/FIRAS determination of the CMB spectrum [60] is based on the absolute CMB signal, which is about 10^5 times larger than the fluctuations that we have considered in this paper.

Figure 1 shows that our map agrees very well with the internal linear combination (ILC) map from the WMAP team on the scales $\gtrsim 1°$ where they can be compared. This is yet another testimony to the high signal-to-noise in the WMAP data and to the fact that unpolarized CMB foregrounds are manageable: the basic spatial features of the CMB are insensitive to the details of the foreground removal method used.

The basic advantage of our map is illustrated in Fig. 12, which compares its all-sky power spectrum with that of the WMAP team ILC map. Both power spectra have had beam effects removed here; in Fig. 1, our map is shown at the

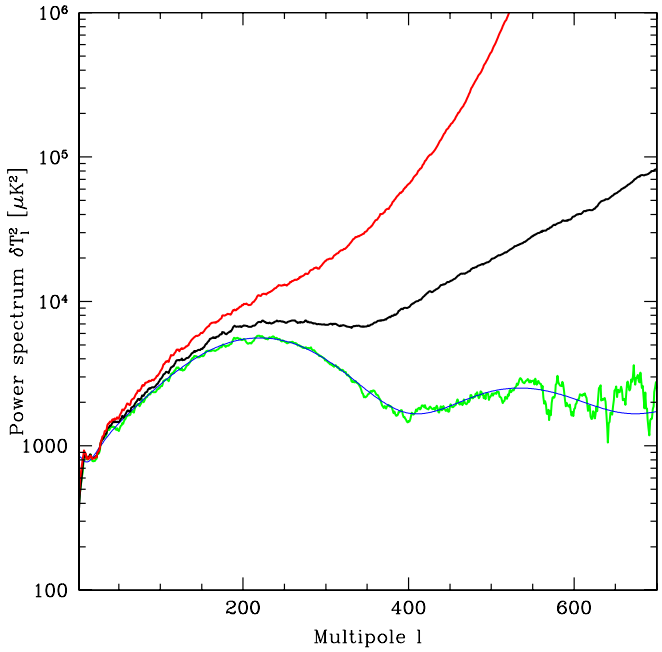

FIG. 12. Comparison of the total (CMB+foregrounds+noise) power spectra of the WMAP team internal linear combination map [3] (top curve) and our cleaned map (middle curve), both for our cleanest sky region. Both of these cleaned maps are seen to reproduce on large scales the CMB power spectrum measured by the WMAP team [6] (lower wiggly curve), which has no net noise contribution because it is based on cross-correlations between channels. The lower smooth curve is the WMAP team's best fit model [17,18]. As explained in the text, the noise contribution is seen to become important earlier in the WMAP team's cleaned map than in ours because it is limited by the lowest resolution frequency bands. All power spectra have been smoothed with a boxcar filter of width $\Delta\ell=10$ to reduce scatter.

W-band resolution and the ILC map is shown at 1° resolution as released.

The first thing to note from Fig. 12 is that foregrounds appear highly subdominant in both maps, since their power spectra essentially coincide with the WMAP CMB power spectrum on large scales where noise becomes unimportant. Second, as expected, the main improvement in our map is seen to be on the smaller scales where noise is important, gaining a factor of 30% at the first acoustic peak and about a factor of two at the second peak where noise from the low frequency channels is beginning to exponentially dominate the ILC map.

We hope that our map will prove useful for a variety of scientific applications. For cross-correlation with external maps, its lowered noise power should be particularly advantageous for pulling out small-scale signals, for instance those associated with lensing and SZ clusters. Rather that attempting detailed modeling of the residual noise and foreground fluctuations in our map, a simple way to place error bars on such correlations will be repeating the analysis with a suite of rotated and flipped versions of our map as in, e.g., [61].

Let us close by returning from small to large angular scales. The surprisingly small CMB quadrupole has intrigued the cosmology community ever since if was first observed by COBE/DMR [62], and simulations by [17,18] show that the low value observed by WMAP is sufficiently unlikely to warrant serious concern. The WMAP team measured the quadrupole using only the part of the sky outside of their Galactic cut, and stress that the dominant uncertainty in its value is foreground modeling. While we agree with this assessment, it should be borne in mind that noise variance and beam issues are completely negligible on these huge angular scales, so this does not imply that the foreground uncertainties are large compared to the signal itself. Indeed, Fig. 12 suggests that foregrounds are subdominant to the intrinsic CMB signal even *without any Galaxy cut* if a foreground-cleaned map is used. While the reader may feel disturbed by the clearly visible Galactic residuals in Fig. 1 (in both the top and bottom maps), it is important to bear in mind that these signals are present in only a tiny fraction of the total sky area and therefore contribute little to the total power spectrum.

To quantify the impact of the Galactic plane, we computed a sequence of all-sky power spectra for both our map and the ILC map. We first used the unadulterated maps, then repeated the calculation after repacing the dirtiest of the nine regions from Fig. 8 with zeros, then zeroed out the 2nd dirtiest region as well, etc. This zeroing procedure obviously biases the measurements by removing power, by an amount related to the zeroed area, but provides a powerful test of how sensitive the results are to Galactic plane details. We also band-pass filtered the resulting maps to produce spatial plots of the quadrupole, octopole and hexadecapole. We found that zeroing out the dirtiest parts of the Galactic plane had a negligible effect on both the power spectrum and on the spatial structure of these lowest multipoles. Specifically, we could zero out all but the three cleanest regions in Fig. 8 (everything with $T>1$ mK) without the quadrupole or octopole changing substantially. The spatial morphology of the quadrupole, octopole and hexadecapole for the all-sky analysis agrees well between our map and the ILC map, again showing insensitivity to galaxy modeling details (in particular, the ILC map is likely to have less contamination in the Galactic plane due to more subdivisions there).

Although more detailed foreground modeling would be needed to rigorously quantify the foreground contribution to low multipoles, let us, encouraged by the above-mentioned tests, tentatively assume that this contribution is unimportant and perform an all-sky analysis of our cleaned map. The resulting power spectrum is shown in Fig. 13, which is simply a blow-up of the leftmost part of the previous figure, and the corresponding angular correlation function is shown in Fig. 14.

Table I summarizes the quadrupole and octopole results. We see that although the quadrupole is still low, it is not quite as low as that from the cut-sky WMAP team analysis of [6]. Moreover, our map has a quadrupole virtually identical to the WMAP team ILC map despite the differences in foreground modeling, further supporting our hypothesis that the quadrupole is not strongly affected by foregrounds. The second column in Table I shows the probability of the quadrupole in our Hubble volume being as low as observed if the best-fit WMAP team model from [17,18] is correct. This is

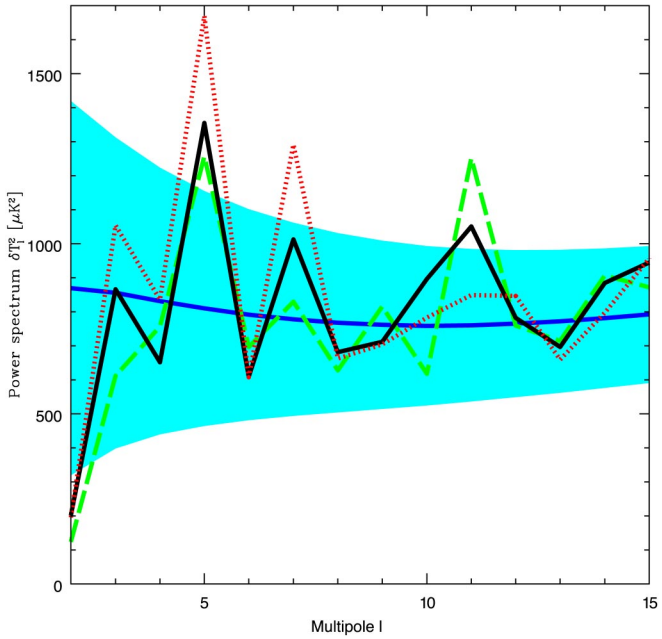

FIG. 13. A heretic all-sky analysis of our cleaned map (solid jagged curve) gives a slightly less low quadrupole δT_2^2 than the cut-sky WMAP analysis [6] (dashed curve), and also agrees well with the quadrupole from an all-sky analysis of the WMAP team cleaned map of [3] (dotted curve). The smooth curve shows the WMAP team best fit model [17,18] with the band indicating the cosmic variance errors (WMAP noise and beam effects are completely negligible on these scales).

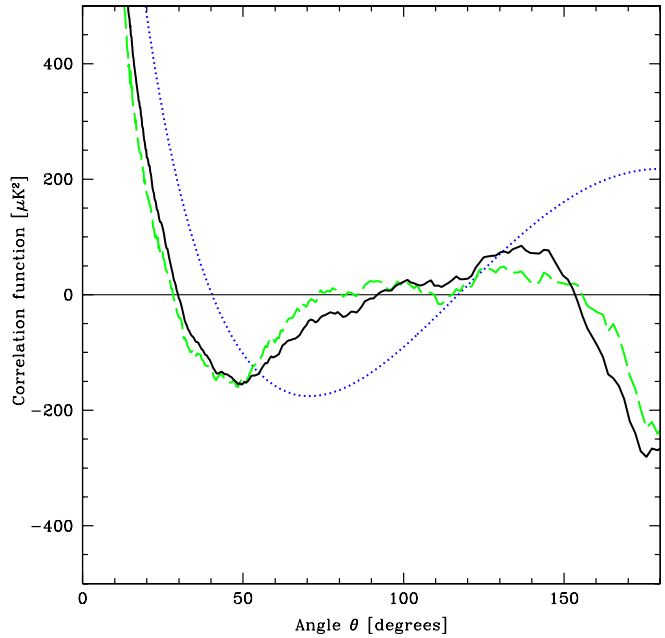

FIG. 14. The angular correlation functions are shown corresponding to our all-sky cleaned map (solid curve), the cut-sky WMAP power spectrum (dashed curve) and the best-fit WMAP team cosmological model (dotted curve). This is simply the Legendre transform of the power spectra from the previous figure, i.e., $(4\pi)^{-1}\Sigma_\ell(2\ell+1)P_\ell(\cos\theta)C_\ell$, so the the quadrupole and octopole contributions are shaped as $3\cos^2\theta-1$ and $5\cos^3\theta-3\cos x$, respectively.

computed for the all-sky case where δT_2^2 has a χ^2-distribution with 5 degrees of freedom, so the probability tabulated is simply $1-\gamma[5/2,(5/2)T_2^2/855.6\ \mu\mathrm{K}^2]/\Gamma(5/2)$, where γ and Γ are the incomplete and complete Gamma functions, respectively.[5] We see that the statistical significance of the low quadrupole problem drops substantially with our all-sky analysis, below the 95% significance level, requiring merely a one-in-twenty fluke.

To understand why the all-sky quadrupole is larger than the cut-sky one measured by the WMAP team, we plot the lowest three multipoles of our cleaned map in Fig. 15, all on the same temperature scale. Several features are noteworthy. First of all, the quadrupole is low with an interesting alignment. A generic quadrupole has three orthogonal pairs of extrema (two maxima, two minima and two saddle points). We see that the actual CMB quadrupole has a strongest pair of lobes that, apparently coincidentally, fall near the Galactic plane. Applying a Galaxy cut therefore removes a substantial fraction of the quadrupole power. The saddle point is seen to be close to zero. In other words, there is a preferred axis in space along which the observed quadrupole has almost no power.

[5]The actual probability is slightly larger for the cut-sky case where there are fewer effective degrees of freedom, although [17] shows with Monte Carlo simulations that there it is still disturbingly small for the measured WMAP quadrupole—indeed, they obtain a consistency probability of 0.7% using Markov chains.

Second, the observed quadrupole is the sum of the cosmic quadrupole and the dynamic quadrupole due to our motion relative to the CMB rest frame—see [63] for a detailed discussion. Since this motion is accurately known from the CMB dipole measurement [1,62], the dynamic quadrupole can and should be subtracted when studying the cosmic contribution. Figure 15 shows the dynamic quadrupole approximated by $(v/c)^2(\cos\theta^2-1/3)$, where $v\approx 369$ km/s towards $(l,b)\approx(264,48)$ is the velocity of the Solar System relative to the CMB [1] and θ is the angle relative to this velocity vector. This is a small correction with peak-to-peak amplitude $(v/c)^2\sim 4\ \mu$K, and Table I shows that it reduces the cosmic quadrupole slightly. This approximation is crude since the dynamic quadrupole in fact depends on frequency [63], and therefore may have been either over- or underestimated in our foreground cleaned map — we have shown it here merely to illustrate its spatial orientation and give an

TABLE I. Measurements of the CMB quadrupole and octopole.

Measurement	δT_2^2 [μK^2]	p-value	δT_3^2 [μK^2]
Spergel *et al.* model	869.7		855.6
Hinshaw *et al.* cut sky	123.4	1.8%	611.8
ILC map all sky	195.1	4.8%	1053.4
Cleaned map all sky	201.6	5.1%	866.1
Cosmic quadrupole	194.2	4.7%	
Dynamic quadrupole	3.6		

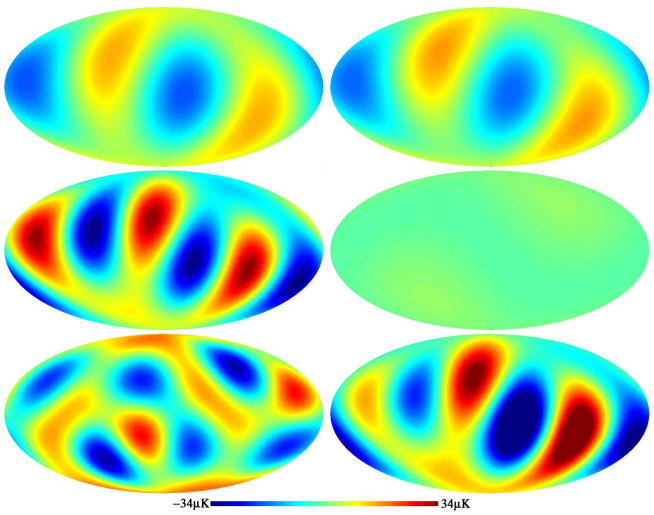

FIG. 15. The left panel shows the quadrupole (top), octopole (middle) and hexadecapole (bottom) components of our cleaned all-sky CMB map from Fig. 1 on a common temperature scale. Note that not only is the quadrupole power low, but both it and the octopole have almost all their power perpendicular to a common axis in space, as if some process has suppressed large-scale power in the direction of this axis. We computed the corresponding images for the WMAP team ILC map as well, and found them to be very similar. The right panel shows the cosmic quadrupole (top) after a correcting for a crude estimate of the dynamic quadrupole (middle) from our motion relative to the CMB rest frame. The bottom right map shows the sum of the quadrupole and octopole maps from the left panel.

order-of-magnitude estimate of its importance.

Third, although the overall octopole power is large, not suppressed like the quadrupole, it too displays the unusual property of a preferred axis along which power is suppressed. Moreover, this axis is seen to be approximately aligned with that for the quadrupole. The reason that our measured octopole in Fig. 13 is larger than that reported by the WMAP team is therefore, once again, that much of the power falls within the Galaxy cut. In contrast, the hexadecapole is seen to exhibit the more generic behavior we expect of an isotropic random field, with no obvious preferred axis.

How significant is this quadrupole-octopole alignment? As a simple definition of preferred axis for an arbitrary sky map, [64] computes the unit vector $\hat{\mathbf{r}}$ around which the angular momentum dispersion $\langle(\hat{\mathbf{r}}\cdot\mathbf{L})^2\rangle = \Sigma_m m^2|a_{\ell m}(\hat{\mathbf{r}})|^2$ is maximized. Here $a_{\ell m}(\hat{\mathbf{r}})$ denotes the spherical harmonic coefficients of the map in a rotated coordinate system with its z axis in the the $\hat{\mathbf{r}}$ direction. The preferred axes $\hat{\mathbf{r}}_2$ and $\hat{\mathbf{r}}_3$ for the quadrupole and octopole, respectively, are

$$\hat{\mathbf{r}}_2 = (-0.2459, -0.3992, 0.8833), \tag{24}$$

$$\hat{\mathbf{r}}_3 = (-0.1113, -0.5055, 0.8556),$$

i.e., both roughly in the direction of $(l,b)\sim(-110°,60°)$ in Virgo. The angle between these two axes is merely 10.3°, and the probability that a random axis falls inside a circle of radius 10.0° around the quadrupole axis is simply the area of this circle over the area of the half-sphere, about 1/66. In other words, if the CMB is an isotropic Gaussian random field, then a chance alignment this good requires about a 1-in-66 fluke. This issue is discussed in greater detail in [64].

What does this all mean? Although we have presented these low multipole results merely in an exploratory spirit, and more thorough modeling of the foreground contribution to $\ell=2$ and $\ell=3$ is certainly warranted, it is difficult not to be intrigued by the similarities of Fig. 13 with what is expected in some nonstandard models, for instance ones involving a flat ''small Universe'' with a compact topology as in [65–70] and one of the three dimensions being relatively small (of order the Horizon size or smaller). This could have the effect of suppressing the large-scale power in this particular spatial direction in the same sense as is seen in Fig. 13. As so often in science when measurements are improved, WMAP has answered old questions and raised new ones.

ACKNOWLEDGMENTS

We thank the WMAP team for producing such a superb data set and for promptly making it public via the Legacy Archive for Microwave Background Data Analysis (LAMBDA).[6] Support for LAMBDA is provided by the NASA Office of Space Science. We thank Krzysztof Górski and collaborators for creating the HEALPIX package [42,43], which we used both for harmonic transforms and map plotting. Thanks to Ed Bertschinger, Hans Kristian Eriksen, Gary Hinshaw, Jim Peebles, Ned Wright and Matias Zaldarriaga for helpful comments. This work was supported by NSF grants AST-0071213, AST-0134999, and AST-0205981, and by NASA grants NAG5-10763 and NAG5-11099. M.T. was supported by the David and Lucille Packard Foundation and the Research Corporation.

[6]The WMAP data are available from http://lambda.gsfc.nasa.gov.

[1] C. L. Bennett *et al.*, Astrophys. J., Suppl. **148**, 1 (2003).
[2] C. L. Bennett *et al.*, Astrophys. J. **583**, 1 (2003).
[3] C. L. Bennett *et al.*, Astrophys. J., Suppl. **148**, 97 (2003).
[4] C. Barnes *et al.*, Astrophys. J., Suppl. **148**, 143 (2003).
[5] C. Barnes *et al.*, Astrophys. J., Suppl. **148**, 51 (2003)
[6] G. Hinshaw *et al.*, Astrophys. J., Suppl. **148**, 135 (2003).
[7] G. Hinshaw *et al.*, Astrophys. J., Suppl. **148**, 63 (2003).
[8] N. Jarosik *et al.*, Astrophys. J., Suppl. **148**, 413 (2003).
[9] N. Jarosik *et al.*, Astrophys. J., Suppl. **148**, 29 (2003).
[10] A. Kogut *et al.*, Astrophys. J., Suppl. **148**, 161 (2003).
[11] E. Komatsu *et al.*, Astrophys. J., Suppl. **148**, 119 (2003).
[12] M. Limon *et al.*, http://lambda.gsfc.nasa.gov/product/map/map_bibliography.cfm (2003).
[13] L. Page *et al.*, Astrophys. J. **585**, 566 (2003).

[14] L. Page *et al.*, Astrophys. J., Suppl. **148**, 39 (2003).
[15] L. Page *et al.*, Astrophys. J., Suppl. **148**, 233 (2003).
[16] H. V. Peiris *et al.*, Astrophys. J., Suppl. **148**, 213 (2003).
[17] D. N. Spergel *et al.*, Astrophys. J., Suppl. **148**, 175 (2003).
[18] L. Verde *et al.*, Astrophys. J., Suppl. **148**, 195 (2003).
[19] H. V. Peiris and D. N. Spergel, Astrophys. J. **540**, 605 (2000).
[20] S. P. Boughn, R. G. Crittenden, and G. P. Koehrsen, Astrophys. J. **580**, 672 (2002).
[21] J. Diego and J. Silk, astro-ph/0302268.
[22] Y. S. Song, A. Cooray, L. Knox, and M. Zaldarriaga, Astrophys. J. **590**, 664 (2002).
[23] A. Cooray, Phys. Rev. D **65**, 103510 (2002).
[24] C. M. Hirata and U. Seljak, Phys. Rev. D **67**, 043001 (2003).
[25] Z. Haiman and G. P. Holder, astro-ph/0302403.
[26] G. Holder, Z. Haiman, M. Kaplinghat, and L. Knox, Astrophys. J. **595**, 13 (2003).
[27] L. Hui and Z. Haiman, Astrophys. J. **596**, 9 (2003).
[28] M. Tegmark and G. Efstathiou, Mon. Not. R. Astron. Soc. **281**, 1297 (1996).
[29] M. Tegmark, D. J. Eisenstein, W. Hu, and A. de Oliveira-Costa, Astrophys. J. **530**, 133 (2000).
[30] A. de Oliveira-Costa *et al.*, Phys. Rev. D **68**, 083003 (2003).
[31] Conf. Ser., Microwave Foregrounds, edited by A. de Oliveira-Costa and M. Tegmark (ASP, San Francisco, 1999).
[32] A. de Oliveira-Costa *et al.*, Astrophys. J. **567**, 363 (2002).
[33] F. R. Bouchet *et al.*, Space Sci. Rev. **74**, 37 (1995).
[34] F. R. Bouchet and R. Gispert, New Astron. **4**, 443 (1999).
[35] F. R. Bouchet, R. Gispert, and J. L. Puget, in *Unveiling the Cosmic Infrared Background*, edited by E. Dwek (AIP, Baltimore, 1996), p. 255; F. R. Bouchet, S. Prunet, and S. K. Sethi, Mon. Not. R. Astron. Soc. **302**, 663 (1999).
[36] M. Tucci, E. Carretti, S. Cecchini, R. Fabbri, M. Orsini, and E. Pierpaoli, New Astron. **5**, 181 (2000).
[37] C. Baccigalupi, C. Burigana, F. Perrotta, G. De Zotti, L. La Porta, D. Maino, M. Maris, and R. Paladini, Astron. Astrophys. **372**, 8 (2001).
[38] C. Burigana and L. La Porta, astro-ph/0202439.
[39] M. Bruscoli, M. Tucci, V. Natale, E. Carretti, R. Fabbri, C. Sbarra, and S. Cortiglioni, New Astron. **7**, 171 (2002).
[40] M. Tucci, E. Carretti, S. Cecchini, L. Nicastro, R. Fabbri, B. M. Gaensler, J. K. Dickey, and N. M. McClure-Griffiths, Astrophys. J. **579**, 607 (2002).
[41] G. Giardino, A. J. Banday, K. M. Gorski, K. Bennett, J. L. Jonas, and J. Tauber, Astron. Astrophys. **387**, 82 (2002).
[42] K. M. Górski, E. Hivon, and B. D. Wandelt, in *Evolution of Large-Scale Structure*, edited by A. J. Banday, R. S. Sheth, and L. da Costa (PrintPartners Ipskamp, The Netherlands, 1999), p. 37.
[43] K. M. Górski, B. D. Wandelt, F. K. Hansen, and A. J. Banday, astro-ph/9905275.
[44] E. L. Wright *et al.*, astro-ph/9601059.
[45] M. Tegmark, Astrophys. J. Lett. **480**, L87 (1997).
[46] P. Natoli, P.F. Muciaccia, and N. Vittorio, Astrophys. J. Lett. **488**, L63 (1997).
[47] L. Knox, Phys. Rev. D **52**, 4307 (1995).
[48] M. Tegmark, Astrophys. J. **502**, 1 (1998).
[49] E. Hivon, K. M. Górski, C. B. Netterfield, B. P. Crill, S. Prunet, and F. Hansen, Astrophys. J. **567**, 2 (2002).
[50] J. E. Ruhl, astro-ph/0212229.
[51] M. Tegmark, Phys. Rev. D **55**, 5895 (1997).
[52] N. Wiener *Extrapolation and Smoothing of Stationary Time Series* (Wiley, New York, 1949).
[53] G. B. Rybicki and W. H. Press, Astrophys. J. **398**, 169 (1992).
[54] O. Lahav *et al.*, Astrophys. J. Lett. **423**, L93 (1994).
[55] K. B. Fisher *et al.*, Mon. Not. R. Astron. Soc. **272**, 885 (1995).
[56] S. Zaroubi *et al.*, Astrophys. J. **449**, 446 (1995).
[57] J. Bond, Phys. Rev. Lett. **74**, 4369 (1995).
[58] E. F. Bunn, Y. Hoffmann, and J. Silk, Astrophys. J. **464**, 1 (1996).
[59] M. Tegmark *et al.*, Astrophys. J. Lett. **474**, L77 (1996).
[60] J. Mather *et al.*, Astrophys. J. **420**, 439 (1994).
[61] A. de Oliveira-Costa *et al.*, Astrophys. J. Lett. **509**, L9 (1998).
[62] G. F. Smoot *et al.*, Astrophys. J. Lett. **396**, L1 (1992).
[63] M. Kamionkowski and L. Knox, Phys. Rev. D **67**, 063001 (2003).
[64] A. de Oliveira-Costa, M. Tegmark, M. Zaldarriaga, and A. J. S. Hamilton, astro-ph/0307282.
[65] N. N. Starobinsky, JETP Lett. **57**, 622 (1993).
[66] D. Stevens, D. Scott, and J. Silk, Phys. Rev. Lett. **71**, 20 (1993).
[67] A. de Oliveira-Costa and G. F. Smoot, Astrophys. J. **448**, 477 (1995).
[68] A. de Oliveira-Costa, G. F. Smoot, and A. A. Starobinski, Astrophys. J. **468**, 457 (1996).
[69] J. Levin, Phys. Rep. **365**, 251 (2002).
[70] G. Rocha *et al.*, astro-ph/0205155.